Journal of Materials Chemistry A

ROYAL SOCIETY OF CHEMISTRY

PAPER

View Article Online
View Journal | View Issue

Cite this: J. Mater. Chem. A, 2024, 12, 19935

Microstructural and electron framework-engineered 3D NiSeP-integrated CuFe composites as trifunctional electrocatalysts for sensing and urea-assisted water-splitting applications†

Ameer Farithkhan,[a] N. S. K. Gowthaman,[*b] Raju Suresh Kumar,[c] Krishnapandi Alagumalai,[d] Wei Sea Chang[*b] and Sankaran Meenakshi[*a]

Received 21st March 2024
Accepted 4th June 2024

DOI: 10.1039/d4ta01919a

rsc.li/materials-a

The development of catalytically dynamic, self-supporting, and cost-effective electrodes equipped with efficient trifunctional catalytic microarchitectures is pivotal in addressing the emerging demands of the healthcare and energy sectors. For the first time, this research reports the strategic integration of three-dimensional Se and P-fused NiSeP (NSP) microflakes with CuFe (CF) composite cubes anchored over an inherently capacious nitrogen-doped carbonized wood (NCW) (NSP-CF@NCW) and explores the impact of diverse strategies of electron and microstructural engineering of electrocatalytic sites on the trifunctional performances for enzyme-free urea sensing and urea electrolysis. Among the array of built electrodes, the NSP-CF@NCW electrode exhibits excellent multifaceted electrocatalysis ability triggered by the synergistic effects of highly voluminous and interconnected NSP flakes anchored over the CF composite, which results in unique electron channeling for efficient electrocatalytic kinetics. The NSP-CF@NCW electrode as a urea sensor exhibits momentous sensitivities of 33.1 and 7.0 mA mM^{-1} cm^{-2} accompanied with the corresponding broad linear ranges of 0.01–0.5 mM and 0.5–9.0 mM, respectively, and a detection limit of 0.0085 mM (S/N = 3). Moreover, as a urea electrolyzer, the best-performing electrode requires an overpotential of 1.49 V to deliver a high current density of 50 mA cm^{-2}, which is 210 mV lower than that required for the standard alkaline water splitting reaction.

Introduction

The sustainable progression of humankind is now closely intertwined with the simultaneous advancement of the personal healthcare domain through the integration of economically viable, resilient, and rapid biomolecule sensing technologies and the energy landscape that is seamlessly capable of assimilating renewable and green energy provisions.[1–3] Over the last decade, the domain of biosensors has witnessed a rapid advancement in the monitoring and early screening of countless life-threatening conditions caused by the abnormal levels of important biomolecules in the human body. Urea is a principal end-product of protein catabolism and plays a crucial role as a key indicator in assessing the dynamic functioning of the kidney and liver.[4,5] The standard physiological level of urea in the human body ranges between 2.6 and 6.5 mM, and any deviation from this ideal level such as high concentrations might be associated with severe health complications comprising chronic kidney disease, gastrointestinal bleeding, urinary tract obstruction, shock, and dehydration, whereas low levels of urea cause cachexia, hepatic failure, and nephrotic syndrome.[6–8] Thus, it is greatly essential to develop a rapid, simple, and efficient tool to identify and prevent the abovementioned serious health issues caused by abnormal urea levels.

Electrochemical urea sensors have demonstrated promising urea sensing capabilities with effective selectivity, ease of on-site assessment, and improved shelf-life. Accordingly, enzyme-free urea sensors (EFUSs) in recent years have attracted deep attention from researchers owing to their beneficial features such as high sensitivity and selectivity, ease of fabrication, simple operation, excellent reproducibility, concrete stability, anti-interference capabilities, and low cost.[9–11] Despite the ample research endeavors explored in the landscape of EFUSs, the utilization of stereotypical current collectors such as glassy

[a]Department of Chemistry, The Gandhigram Rural Institute-Deemed to be University, Gandhigram 624302, Tamil Nadu, India. E-mail: sankaranmeenakshi2014@gmail.com

[b]School of Engineering, Monash University, Bandar Sunway, Selangor 47500, Malaysia. E-mail: gowthaman.nalla@monash.edu; chang.wei.sea@monash.edu

[c]Department of Chemistry, College of Science, King Saud University, P.O. Box 2455, Riyadh 11451, Saudi Arabia

[d]School of Chemical Engineering, Yeungnam University, Gyeongsang 38541, Republic of Korea

† Electronic supplementary information (ESI) available. See DOI: https://doi.org/10.1039/d4ta01919a

carbon, gold, and platinum electrodes require electronically insulating binders for the effective attachment of electroactive urea sensing materials. This approach not only augments the overall cost of electrode fabrication but also limits the efficiency of the sensor by triggering the impeded electron transfer between the current collector and the support; besides, their instability under electrochemical cycling and non-disposable behavior bring complexities in their practical implementation.[12–14] Thus, directly decorating the surface of sustainable and renewable current collectors with highly active electrocatalytic materials is promising for the fabrication of EFUSs capable of performing effective urea assessment *via* inducing the urea oxidation reaction (UOR) on the active catalytic surface.

Biomass wood has recently attracted immense attention as a potential candidate for the construction of a highly conductive, eco-friendly, cost-efficient, and robust catalyst support that is naturally built with inherent three-dimensional (3D) porous multi-channels providing sufficient surface area for docking electroactive catalytic materials. This environmentally benign natural biopolymer can be readily converted into advanced carbon supports *via* a high-temperature carbonization process and functionalized by facile *in situ* nitrogen doping to establish momentous surface wettability.[15–18] Therefore, the binder-free decoration of catalytic materials over the hollow carbon multi-channels of nitrogen-doped carbonized wood (NCW) electrodes obtained *via* the high-temperature pyrolysis of renewable raw wood would be highly promising for the construction of effective EFUSs.

On the flip side, the rapidly growing energy demands and the exhaustion of fossil fuel sources by polluting the environment have inspired researchers to urgently develop practically viable eco-friendly energy technologies.[19–21] Electrochemical water splitting (EWS) involving hydrogen evolution reaction (HER) and oxygen evolution reaction (OER), respectively occurring at the cathode and anode has been proven to hold great potential to meet the ever-growing energy needs by providing hydrogen as the promising and sustainable energy carrier.[22,23] However, concerning these two half-cell reactions, the OER ($4OH^- \rightarrow 2H_2O + O_2 + 4e^-$) at the anode requires a higher overpotential than its theoretical ideal value (1.23 V *versus* reversible hydrogen electrode, labeled as RHE) owing to its sluggish dioxygen formation kinetics, which hinders the wide-spread practical implementation of EWS.[24,25] Consequently, substituting the sluggish OER with the more thermodynamically and kinetically favorable advanced anodic reactions employing other small molecules is revolutionary in light of promoting power-to-gas technology to produce the environmentally benign fuel. The UOR ($CO(NH_2)_2 + 6OH^- \rightarrow N_2 + CO_2 + 5H_2O + 6e^-$) has recently gained momentum in the landscape of energy-efficient H_2 production owing to its encouraging ultra-low theoretical voltage (0.37 V *vs.* RHE), global abundance, nonflammability, nontoxicity, ease of transportation and storage.[26–28] However, regardless of the aforementioned advantages, considerable attention should be paid to tap the momentous potential of UOR-assisted water splitting by developing and advancing a highly active catalytic system to realize the vision of energy-efficient and cost-viable H_2 production.

Among the various precious/non-precious electrocatalysts, nickel-based catalytic structures have been extensively studied as remarkable UOR-active materials owing to the facile formation of bridged conformation between urea and catalytically active Ni^{3+} triggered by its alliance with vacant d-orbitals. In addition, through experimental observations, Botte *et al.* found that the formation potential of Ni^{3+} from the Ni^{2+} phase in an alkaline environment is nearly located at the electrolysis potential of urea.[29,30] However, the aforementioned monometallic Ni-based electrocatalysts deliver limited UOR kinetics owing to the elevated onset potential, thermodynamic instability of the catalytically dynamic Ni^{3+} phase, elevated surface poisoning effect, and inferior chemical robustness during electrochemical cycling in a harsh alkaline medium. Thus, the fabrication of UOR electrocatalysts with optimal multi-elemental and multi-interfacial architectures that hold the potential to eliminate the abovementioned technical barriers toward momentous UOR by demonstrating encouraging leaps in elevated electrocatalytic activity is highly indispensable.

Accordingly, in recent years, transition metal selenides (TMSs) exhibiting excellent structural and material properties have set a promising benchmark for remarkable electrocatalytic performances in distinct realms of electrochemical applications. Mainly, the analogies observed in the electronic architecture of selenium (Se) 3d orbitals with 3s and 3p orbitals of transition metal atoms endow strong metal-like properties to TMSs, which embarks their high electronic conductivity, lower energy band, and momentous redox activity.[31–33] Despite these significant advantages, the inferior exposed active sites and critical corrosion followed by dissolution in harsh electrolyte environments severely hampers TMS's efficiency towards achieving excellent electrochemical activity and concrete cycling stability.[34] Amid the various strategies employed to amplify the competent redox capability and long-term stability of TMSs, including defect engineering, morphological tuning, and phase modification, tailoring of the electrocatalytic surface with heteroatom decoration, particularly with phosphorus (P) atoms, has been a promising strategy to manipulate the electronic environment as well as introducing the synergistic dual anion effect targeted towards marked augmentation of catalytic activity and stability, simultaneously.[35] The incorporation of P atoms with an inherent Pt mimicking electron framework equipped with high-valance state re-engineers the electronic architecture of TMS by modulating the Fermi-level and d-band center of metal atoms and plays a crucial role in elevating the kinetics of electrocatalytic reactions. In addition, the modulation of the electron density around the Se, P-dopants intensifies the strength of the metal–Se bond in TMSs and remarkably enhances its stability characteristics.[36–38]

Moreover, the multicomponent interface engineering of the conductive substrate with electronically active materials to dock the catalytically dynamic structures is deemed to be a favorable approach that affords robust catalyst anchoring sites, maximizes the exposed surface area, manipulates the electronic

architecture of active structures and enhances the remarkable electron transfer characteristics for a targeted electrochemical reaction. In principle, at the catalytic site, the process of dynamic reaction occurs *via* the rapid adsorption and desorption of reactants and products, and the electronic framework of such active sites determines the kinetics of the catalytic reaction. Creating a heterointerface between the two electroactive active phases can manipulate the interfacial electronic environment by inducing the re-distribution of electrons and amplifying the density of available catalytic active sites, thereby promoting the electrocatalytic reaction.[39,40] Researchers also discovered that strong interfacial interaction between two dynamic components can result in novel physiochemical properties such as synergistic electronic effect, activation and stabilization of catalytic active sites, and optimization of the free energy of adsorption and desorption of reaction intermediates and products for efficient electrocatalytic activity.[41] By virtue of the abovementioned advantages, the construction of unique electroactive microarchitectures including discrete heterointerface conjoining the NCW and the catalytically engaged architectures is highly crucial. Not only does this interface serve as a novel catalyst docking platform but it is also capable of engineering the electronic framework of catalytically responsive microstructures that result in the elevation of catalytic activity.

The first-row transition metal oxides, layered double hydroxides (LDH), and mixed-metal composites attract considerable attention from researchers as electroactive materials due to their advantages including effective electron transfer characteristics, ample precursor availability, tunable chemical and electronic frameworks, excellent electronic conductivity, tunable bandgap, and low cost.[42–45] Particularly, in the context of mixed-metal composites, the synergy between the two different electron-rich metal constituents within a bimetallic framework establishes unique electronic and geometrical phenomena that can synergistically control and optimize the demanded electronic architecture when in conjunction with the catalytically active materials. Although diverse mixed-metal composites such as NiFe LDH, NiCo LDH, NiCo nanowire arrays, NiMo nanorods, and CuFe have found applications in distinct electrochemical contexts, there exist no admirable research endeavors focused on employing CuFe bimetallic composites as electron engineering platforms to augment the catalytic activity of the grown electrocatalysts towards UOR.[46–50]

Even though the catalysts hold the potential to simultaneously execute the catalysis of more than one reaction, ample research endeavors focus only on the design and development of electrocatalysts for a single targeted function, and thus, the true multifunctional potential of the fabricated system is left untapped. Recently, plenteous different studies of these trifunctional electrocatalysts were reported in detail by Balogun and co-workers including catalysts for overall water splitting and diverse battery technologies.[51–54] These reports profoundly validate the importance of trifunctional electrocatalysts in the rapidly blooming energy sector. The construction of multifunctional electrocatalysts not only remarkably simplifies the process of design and advancement of a single catalytic material for more than one purpose but also reduces the cost of catalyst fabrication, conserves energy, and paves the path for the commercialization of impressive electrochemical technologies. Consequently, for the first time in the literature, this research reveals the strategic integration of 3D Se and P-decorated NiSeP (NSP) microflakes with CuFe (CF) composite cubes directly docked over the capacious carbon multi-channels of NCW scaffolds (NSP-CF@NCW) (Fig. 1), and explored the impact of diverse electron framework and microstructural engineering of electrocatalytic sites towards the multifaceted EFUS and urea-assisted water electrolysis. Besides, other control electrodes including NCW, CF@NCW, $Ni(OH)_2$@NCW, $Ni(OH)_2$-CF@NCW, and NiSe-CF@NCW (NS-CF@NCW) electrodes were fabricated. The chemical compositions and microstructural features of the as-constructed binder-less, free-standing, and sustainable trifunctional electrodes were studied with distinct spectroscopic and microscopic techniques. The multi-dimensional electrocatalysis of the prepared electrodes toward the EFUS and urea-assisted water electrolysis is exploited with corresponding electrochemical investigations. The best-performing NSP-CF@NCW electrode exhibits impressive sensitivities of 33.1 and 7.0 mA mM^{-1} cm^{-2}, covering the corresponding linear ranges of 0.01–0.5 mM and 0.5–9.0 mM, with a detection limit of 0.0085 mM (S/N = 3) as a urea sensor. Additionally, to achieve the high current density of 50 mA cm^{-2}, the NSP-CF@NCW electrode requires an overpotential of only 1.49 V, which is 210 mV lower than that required for the stereotypical alkaline water splitting reaction.

Materials and methods

Chemicals

Copper(II) chloride ($CuCl_2$, ≥99.0%), iron(III) chloride anhydrous ($FeCl_3$, ≥99.0%), nickel(II) nitrate hexahydrate ($Ni(NO_3)_2 \cdot 6H_2O$, ≥99.0%), selenium powder (Se, ≥99.0%), sodium hypophosphite monohydrate ($NaH_2PO_2 \cdot H_2O$, ≥99.0%), potassium hydroxide (KOH, ≥90.0%), urea (CH_4N_2O, ≥99.0%), glucose ($C_6H_{12}O_6$, ≥99.0%), uric acid ($C_5H_4N_4O_3$, ≥99.0%), ascorbic acid ($C_6H_8O_6$, ≥99.0%), potassium chloride (KCl, ≥98.0%), sodium chloride (NaCl, ≥99.0%), and ethanol (C_2H_5OH, ≥99.8%) were obtained from Sigma-Aldrich and used without further purification.

Fabrication of the NCW

To fabricate the NCW, waste wood pieces were obtained from a local store and washed with C_2H_5OH and distilled deionized (DDI) water, followed by ambient stirring in a urea suspension for 12 h and drying in a hot-air oven at 80 °C overnight. After the pre-treatment procedures, the wooden pieces were placed in a porcelain boat and transferred into a tubular furnace, which was then air-stabilized at 250 °C for 3 h followed by carbonization at 1000 °C for 2 h at a heating rate of 2 °C min^{-1} protected under a N_2 environment. Without any further treatments, the as-obtained NCWs were employed for the direct anchoring of electroactive structures.

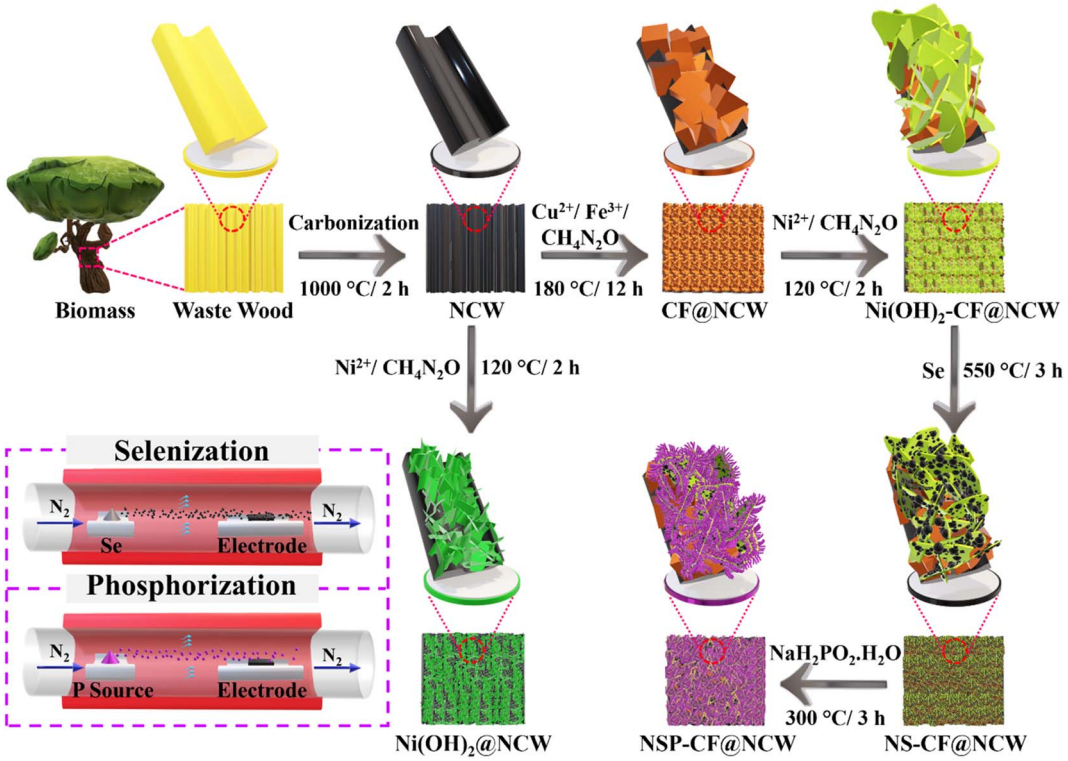

Fig. 1 Schematic representation of NSP-CF@NCW fabrication.

Preparation of NSP-CF@NCW

First, the decoration of the CF composite, $Ni(OH)_2$-CF and $Ni(OH)_2$ microarchitectures over the NCW was executed by following distinct hydrothermal protocols. In the typical synthesis of CF@NCW, $CuCl_2$ (0.3 g) and $FeCl_3$ (0.7 g) were dissolved in DDI water (30 ml) and stirred vigorously for 30 min. Then, urea (0.15 g) was added to the above precursor solution and stirred until a homogeneous solution was obtained. The above final reaction mixture was transferred to a 100 ml Teflon-lined autoclave containing an NCW electrode and maintained in an oven at 180 °C for 12 h. After completion of the reaction, the produced CF@NCW was washed several times with C_2H_5OH and DDI water and dried at 80 °C for 12 h. Similarly, $Ni(NO_3)_2 \cdot 6H_2O$ (0.5 g) was dissolved in DDI water (30 ml) containing urea (0.15 g) and the resulting solution was vigorously stirred for 30 min until a homogeneous pale green solution was obtained. Subsequently, the obtained reaction mixture was poured into a Teflon-lined autoclave loaded with the as-prepared CF@NCW and then kept at 120 °C for 12 h. After allowing the autoclave to cool down to the ambient temperature, the acquired $Ni(OH)_2$-CF@NCW was rinsed multiple times with ethanol and DDI water and dried for 12 h at 80 °C. By replacing the CF@NCW electrode with the unmodified NCW, the aforementioned synthesis procedure was also implemented for the preparation of the $Ni(OH)_2$@NCW electrode.

Following the protocols outlined above, the as-prepared $Ni(OH)_2$-CF@NCW electrode was placed in the downstream region along with the Se powder (0.2 g) kept in the upstream region of the tubular furnace in a porcelain boat. Subsequently, under a N_2 flow (50 sccm), the NS-CF@NCW electrode was obtained by maintaining the reaction temperature of the furnace at 550 °C for 3 h at a heating rate of 2 °C min^{-1}. Finally, the NSP-CF@NCW electrode was prepared in identical assemblies, in which $NaH_2PO_2 \cdot H_2O$ (0.1 g) was placed in the upstream region, whereas the as-prepared NS-CF@NCW was kept in the downstream region. The phosphorization reaction was executed at 300 °C for 3 h under a constant N_2 stream maintained throughout the process. After allowing the furnace to reach the ambient temperature, NSP-CF@NCW was obtained.

Instrumentation

The morphological and elemental characterizations of the prepared electrodes were performed using a VEGA3 TESCAN scanning electron microscope (SEM) equipped with an energy-dispersive X-ray spectrometer (EDX) from Bruker Nano. The electronic and chemical states of the prepared sample were studied by X-ray photoelectron spectroscopy (XPS) carried out using a PHI 5000 VERSAPROBE with an Al Kα excitation source. The phase and crystalline patterns of the constructed electrodes were acquired using an X-ray diffractometer (XRD) (PAN Analytical's Empyrean XRD) equipped with a Cu-Kα radiation (λ = 1.54 Å) source at a current and voltage of 15 mA and 40 kV, respectively. The Raman spectra of the prepared samples were recorded using a confocal Raman microscope equipped with a 532 nm laser excitation source (WiTec alpha 300).

Electrochemical measurements

All the electrochemical examinations including urea detection, UOR, and HER were carried out in a three-electrode setup at

ambient temperature. The experimental setup comprises an electrochemical workstation (CHI-743B) consisting of unmodified and catalyst-decorated NCWs (1 cm × cm) as the working electrode, a Ag/AgCl electrode as the reference, and a Pt rod as the counter electrode. In the presence of 1.0 M KOH and 0.33 M urea + 1.0 M KOH, linear sweep voltammetry (LSV) technique was used to obtain the polarization profiles of the constructed electrodes at a scan rate of 5 mV s^{-1}, and based on the equation, $E_{RHE} = E_{Ag/AgCl} + 0.198\ V + 0.059 \times pH$, the respective potentials were standardized to the RHE. Under alkaline conditions, an investigation into the urea-assisted water electrolysis was carried out with commercial urea, human urine, domestic wastewater, and agricultural wastewater using a two-electrode setup consisting of the as-constructed electrode as both the anode and the cathode. The systematic electrochemical assessments were repeated until consistent results were obtained.

Results and discussion

Morphological characterization

The characteristic surface morphologies of bare NCW and catalyst-docked electrodes were explored by SEM and illustrated in Fig. 2A–F″. Fig. 2A and A′ portray the bare NCW electrode inherently built with ample 3D open micro-vessels that are well aligned and extended towards the tree growth direction. The high-magnification SEM image of NCW (Fig. 2A″) depicts the well-aligned hollow carbon micro-channels with the mean diameter and wall thicknesses of 8.6 and 2.8 μm, respectively, furnishing a plenteous room for anchoring catalytically dynamic microarchitectures, and thereby meeting the crucial design standards for the fabrication of competent electrocatalytic electrodes. The extensive SEM examinations of the catalyst-modified electrodes, as depicted in Fig. 2B–F″, reveal the systematic executions of microstructural engineering on catalytic architectures aimed to augment the electrocatalytic trifunctionality of the constructed electrodes. The low-magnification SEM assessments of $Ni(OH)_2$@NCW (Fig. 2B and B′) illustrate the uniform envelopment of $Ni(OH)_2$ flakes hydrothermally anchored over the NCW support, whereas the magnified scrutiny (Fig. 2B″) displays the formation of highly interconnected, wrinkled, and thin $Ni(OH)_2$ flakes protruding from the core contributing significant reactive room for the targeted electrochemical reaction. Fig. 2C–C″ show the uniformly and densely grown CF microcubes well wrapped over the surface of NCW in a fused fashion, creating a well-connected network configuration for effective electron-transfer characteristics. The high magnification SEM analysis (Fig. 2C″) reveals the intricacies of CF@NCW, which displays smooth surfaced CF composite cubes with a mean edge length of 0.36 μm rooted and grown vertically from the nucleation point on the NCW. This geometric microstructural foundation serves as an electron-manipulating platform to modulate the electronic framework of catalytically active structures.

In succession to the above, the hydrothermal treatment of CF@NCW under the Ni source orchestrates the integration of uniformly decorated thin, abundantly fused, and relatively smoother $Ni(OH)_2$ flakes oriented vertically atop the CF cubes (labeled as $Ni(OH)_2$-CF@NCW) (Fig. 2D–D′). As shown in Fig. 2D″, the cross-stacked $Ni(OH)_2$ flaky walls docked over the CF cubes adjoined together constructing a 3D highly porous and voluminous interspaces with a mean diameter of 1.2 μm. In addition to the electronic engineering that augments the electron transport kinetics, this strategically developed structural configuration of $Ni(OH)_2$-CF@NCW concurrently provides ample room for remarkable diffusion and electrooxidation of urea. Moreover, it contributes to structural integrity that

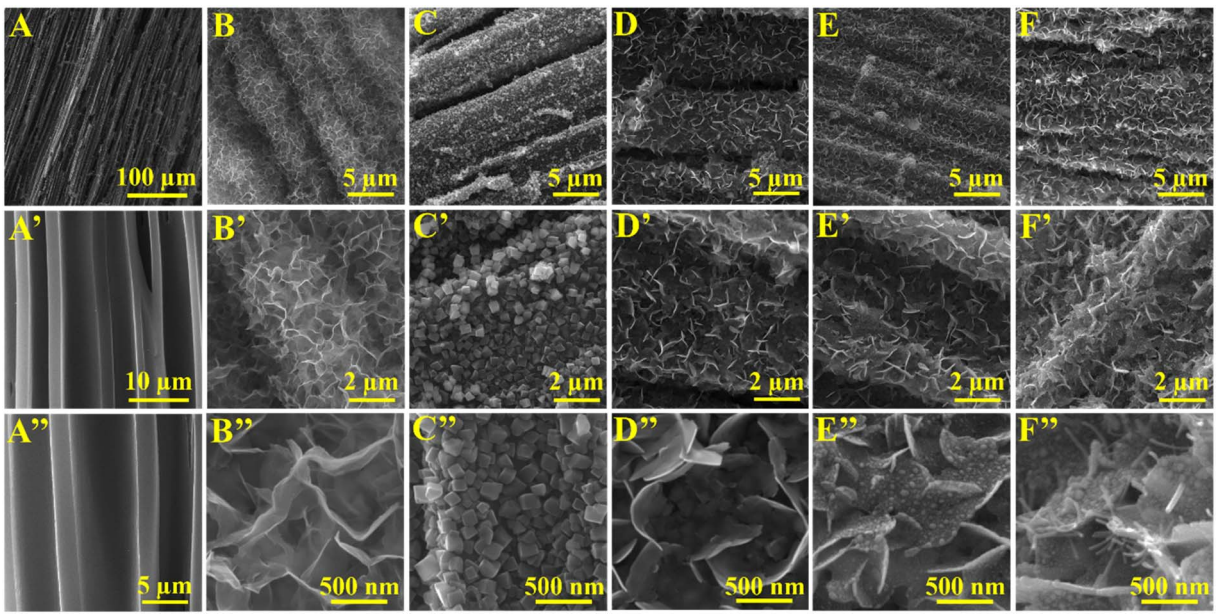

Fig. 2 SEM images of (A–A″) naked NCW, (B–B″) $Ni(OH)_2$@NCW, (C–C″) CF@NCW, (D–D″) $Ni(OH)_2$-CF@NCW, (E–E″) NS-CF@NCW and (F–F″) NSP-CF@NCW at different magnifications.

eliminates the aggregation and sintering of 2D flakes during the course of electrochemical procedures. Fig. 2E–E″ illuminate the structural evolution of $Ni(OH)_2$-CF@NCW after the selenization procedure, in which the smooth and flourished walls of $Ni(OH)_2$ flakes were homogeneously implanted with sphere-like structural motifs. Obviously, the event of selenization provoked an elevation in the exposed surface roughness of NS-CF@NCW, thereby facilitating the enhancement in electrocatalytic performance. Following the above, during the phosphorization process, the P constituents manifested the emergence of blunt and curved spines that extend prominently over the edges of both sides of NS flakes, imposing a distinctive cactus-like morphology (Fig. 2F–F″). The integration of Se and P concurrently modulated the electron framework of NSP-CF@NCW and also upsurged the surface roughness of exposed catalytically active structures. Astonishingly, despite the events of Se and P doping mediated by the high-temperature conditions, the NSP-CF@NCW electrode outstandingly retained its structural integrity and demonstrated its concrete interfacial construction. Fig. S1 and S2† illustrate the elemental analysis of NSP-CF@NCW, which confirmed the presence of C, N, O, Cu, Fe, Ni, Se, and P.

Characterization by XPS, XRD, and Raman spectroscopy

To further investigate the surface electronic architecture and chemical valences of the as-prepared electrodes, XPS studies were conducted. Fig. 3A reveals the wide-scan survey spectrum, which depicts the presence of C 1s, N 1s, O 1s, Cu 2p, Fe 2p, Ni 2p, Se 3d, and P 2p signals on the surface of the fabricated electrode. Fig. S3A–C† disclose the high-resolution core-level signals of the C 1s, N 1s, and O 1s profiles. The narrow scan C 1s spectrum (Fig. S3A†) shows three distinct peaks at 284.3, 285.4, and 287.9 eV, assigned, respectively to the C–C/C–H, C–O/C–N, and C=O/C=N chemical bonds, which endorses the association of carbon with N and O constituents.[55] The incorporation of N atoms into the carbon framework of NCW was depicted in the high-resolution N 1s spectrum (Fig. S3B†), which reveals the three binding energy (BE) values ascribed to the pyridinic-N, pyrrolic-N, and graphitic-N bonds positioned at 397.9, 398.8 and 401.1 eV, respectively.[56] The O 1s core-level spectrum (Fig. S3C†) was resolved into two peaks signifying the chemical bonds of C=O, and C–O–C/C–OH functionalities corresponding to the BE values positioned at 530.1, and 531.8 eV.[55] As displayed in Fig. 3B, the deconvoluted Cu 2p spectrum of the NSP-CF@NCW electrode portrays the XPS signals at 934.2 and 942.3 eV, which are indexed to Cu $2p_{3/2}$ and its satellite signal, respectively, while the BEs at 953.9 and 962.7 eV can be fitted to the corresponding Cu $2p_{1/2}$ spectrum and its shakeup satellite of Cu^{2+} state.[57] In the narrow-scan spectrum of Fe 2p (Fig. 3C), the bands centered at 711.3 and 724.5 eV fitted the BEs of Fe $2p_{3/2}$ and Fe $2p_{1/2}$ of Fe^{3+}, respectively, and validated its presence in the fabricated electrode, whereas the BE values positioned at 716.1 and 729.8 eV represent satellite signals.[58]

Fig. 3D portrays the comparative high-resolution Ni 2p profiles of catalyst-modified electrodes, which disclose the existence of strong electron-level interactions caused by the multi-elemental and interfacial engineering, as evidenced by upshifts and downshifts in their BE values. The core-level Ni 2p spectrum of $Ni(OH)_2$@NCW displays two pairs of XPS signals featuring Ni–OH bonds and validating the formation of $Ni(OH)_2$ microarchitectures over the carbon support. The BEs found at 855.95 and 873.81 eV can be assigned to the chief spin–orbit Ni $2p_{3/2}$ and Ni $2p_{1/2}$ bands, whereas the other two bands positioned at 861.67 and 879.91 eV are assigned to their corresponding satellite signals.[59] After anchoring $Ni(OH)_2$ over the CF composite cubes, the BE values of Ni $2p_{3/2}$ and Ni $2p_{1/2}$ of $Ni(OH)_2$-CF@NCW distinctly downshifted about 0.37 and 0.40 eV, respectively, towards the lower BE values in contrast to $Ni(OH)_2$@NCW, demonstrating the substantial electron transfer from the CF composite to $Ni(OH)_2$ that increased the electron density of Ni, thereby significantly modulating its electronic framework. Such momentous electron-level engineering executed by facile interfacial engineering may trigger

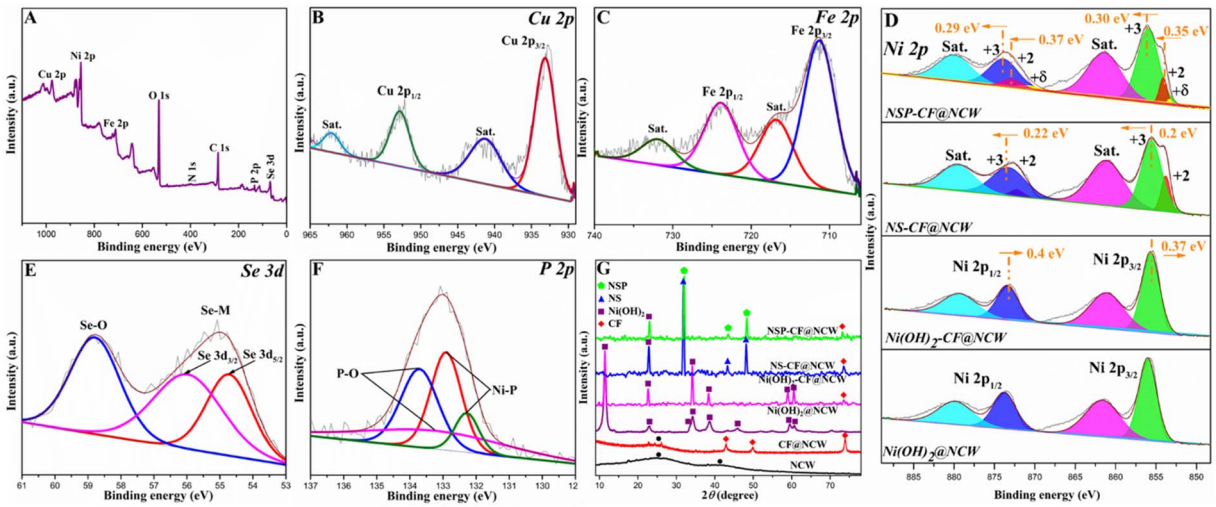

Fig. 3 XPS plots of (A) survey spectrum, and the deconvoluted profiles of (B) Cu 2p, (C) Fe 2p, (D) Ni 2p (compared with other Ni modified NCWs), (E) Se 3d, and (F) P 2p of NSP-CF@NCW. (G) Comparative XRD profile of bare and modified electrodes.

the augmentation of desired electrocatalytic activity. Astonishingly, the incorporation of Se into the Ni framework significantly reconstructed the electronic architecture of NS-CF@NCW featuring the multi-oxidation states involving the chief spin–orbit doublets ascribed to Ni $2p_{3/2}$ and Ni $2p_{1/2}$ of Ni^{3+} state positioned at 855.78 and 873.63 eV, while the peaks centered at 853.78 and 872.31 eV can be indexed to Ni $2p_{3/2}$ and Ni $2p_{1/2}$ of the Ni^{2+} phase. Besides, these chief spin–orbit signals of core-level Ni 2p including Ni $2p_{3/2}$ and Ni $2p_{1/2}$ were primarily upshifted distinctly (0.20 and 0.22 eV, respectively) towards a higher binding energy than that of $Ni(OH)_2$-CF@NCW, which further validates that Se incorporation into the NS-CF@NCW electrode establishes the environment of higher valency in the Ni framework, and regulates its electronic structure towards the amplified electrocatalytic kinetics. It can be visually evidenced that, after P doping, the spin-energy peaks of Ni 2p in NSP-CF@NCW display a positive shift in BE values of ~0.3 eV (Ni $2p_{3/2}$ and Ni $2p_{1/2}$ of Ni^{3+} state shifted to 856.08 and 873.92 eV, while the peaks of Ni $2p_{3/2}$ and Ni $2p_{1/2}$ of Ni^{2+} phase were shifted to 854.13 and 872.68 eV), manifesting surplus intensification of high-valent Ni species, which can be concurrently evidenced by the increase and decrease in Ni^{3+} and Ni^{2+} intensities, respectively. In addition to the above, the two new XPS signals appearing in the Ni 2p profile of NSP-CF@NCW at 853.23 and 870.29 eV are assigned to $Ni^{\delta+}$, which represents the establishment of the Ni–P bond and strongly marks the electronic interaction between Ni and P, benefitting the improved trifunctional electrocatalysis. The deconvoluted profile of Se 3d (Fig. 3E) shows two strong peaks located at 54.73 and 56.05 eV, which can be indexed to Se $3d_{5/2}$ and Se $3d_{3/2}$ of the Se–M bond, respectively. Besides, owing to the surface oxidation of Se, a peak at 58.84 eV of Se–O species was observed.[60] Further, the narrow scan spectrum of P 2p of NSP-CF@NCW (Fig. 3F) exhibits well-defined peaks at 132.28 and 132.91 eV ascribed to the Ni–P species, while other peaks positioned at 133.24 and 133.96 eV can be assigned to P–O species aroused by the exposure to surface oxidation.[61] Accordingly, from the above-mentioned XPS investigation, we can infer that the interfacial engineering of $Ni(OH)_2$ over the CF composite critically manipulated the dynamic electron architecture by augmenting the electron density around Ni species and ultimately amplifying the electron transfer characteristics, while the multi-elemental non-metallic engineering of the Ni framework with Se and P augmented the catalytically demanded high-valent active species, leading to the elevated activity of the constructed electrode toward the desired electrocatalytic trifunctionality. Taken together, the above-mentioned major findings also indicate that NSP-CF@NCW was fabricated successfully.

To examine the crystallographic patterns of the as-prepared electrodes, XRD analysis was performed, and the results are displayed in Fig. 3G. The XRD pattern of the NCW scaffold shows two characteristic diffraction peaks at 2θ of 25.4° and 43.1°, corresponding to the (002) and (100) planes of graphitic carbon framework. The CF@NCW sample exhibits strong diffraction patterns positioned at 43.3°, 50.1°, and 74.1°, which can be well assigned to the (111), (200), and (220) planes, insisting the formation of phase pure CF composites (JCPDS no. 04-0836) over the NCW substrate.[62] The crystallographic patterns of $Ni(OH)_2$ decorated over the NCW are located at the 2θ values of 11.3°, 22.7°, 33.5°, 34.1°, 38.7°, 45.8°, 59.5° and 61.1°, which can be indexed to the (003), (006), (101), (012), (015), (018), (110) and (113) planes of the $Ni(OH)_2$ phase (JCPDS no. 38-0715).[63] The $Ni(OH)_2$-CF@NCW electrode portrays the XRD profile that encompasses the combination of $Ni(OH)_2$ and CF composite crystallographic patterns, which affirms the successful docking of the former flakes over the later cubes. After the selenization process, three new diffraction patterns positioned at 2θ of 32.3°, 43.9°, and 48.9° are detected, which are well matched with the (101), (102), and (110) planes of NiSe (JCPDS no. 75-0610) in the NS-CF@NCW electrode. As shown in Fig. 3G, further P-doping in NSP-CF@NCW disclosed the similar lattice patterns of NS-CF@NCW including a slight positive shift (Fig. S4†) to higher diffraction angles attributed to the crystal lattice expansion triggered by P incorporation.[35,64] This shows that without altering the phase identity, P was successfully incorporated into NSP-CF@NCW.

Furthermore, Raman spectroscopy was performed to acquire information about the polarization-driven vibrational fingerprints of bare and catalyst-modified NCWs. Fig. S5B† presents the Raman spectrum depicting the characteristic properties of the carbon matrix existing in the fabricated electrodes. As pictured in the plot, the strong peaks positioned around 1579 and 1340 cm^{-1} confirm the presence of a G-band of graphitic carbon and a D-band of defective carbon in the fabricated electrodes, respectively.[65] The ratio of the D and G bands (I_D/I_G) was found to be 0.81, which represents the high degree of graphitization of the carbon architecture. Fig. S5A† shows the vibrational properties of catalytic active microstructures docked over the NCW. The Raman bands positioned at 215, 280, 395, 501, and 598 cm^{-1} denote the characteristic lattice vibrational modes of the CF composite in CF@NCW, caused by the typical vibrational features of Fe in its oxide phase allied with the Raman inactivity of Cu.[66] For the $Ni(OH)_2$@NCW electrode, the existence of peaks around 310 and 450 cm^{-1} denotes the Raman signals of $Ni(OH)_2$ microstructures docked over the NCW support.[67] It can be observed that both the characteristic Raman signals of $Ni(OH)_2$ and CF composite coexisted in the profile of $Ni(OH)_2$-CF@NCW, indicating the successful decoration of $Ni(OH)_2$ flaky microarchitectures over the CF composite. As shown in the spectrum of NS-CF@NCW, the vibrational signals appeared around 154, 220, and 242 cm^{-1} representing the phonon modes of Ni–Se in NS, whereas the minor peaks around 208 and 271 cm^{-1} can be assigned to the vibrational modes of the Se–Se pair.[68,69] Further, NSP-CF@NCW portrays the Raman signals around 165, 210, and 145 cm^{-1} ascribed to the vibrational modes of A_{1g} and E_g, respectively, which confirms the successful incorporation of P-atoms.[70]

Electrochemical performance of the fabricated electrodes towards urea sensing

The electrochemical performance of all the constructed electrodes towards the EFUS was investigated in the electrolyte of

0.1 M KOH with the absence and presence of 2 mM urea at a scan rate of 50 mV s^{-1}. Fig. 4A shows the cyclic voltammograms (CVs) of the constructed bare and modified NCWs, which illustrate their redox activity in an alkaline environment. As shown in the CV profile, the unmodified NCW and CF@NCW electrodes demonstrated insignificant redox behavior owing to the inexistence of the catalytically demanding electroactive species. Conversely, the catalyst-anchored electrodes equipped with Ni microstructures displayed noteworthy electrochemical performance allied with the reversible transformation of Ni(OOH) (Ni^{3+})/$Ni(OH)_2$ (Ni^{2+}) couple mediated by the OH^- ions. Under alkaline conditions, the $Ni(OH)_2$@NCW probe displays a well-defined anodic (E_{pa}) response at 0.57 V *vs.* Ag/AgCl, whereas the interface-engineered $Ni(OH)_2$-CF@NCW electrode delivered enhanced current behavior positioned at E_{pa} of 0.55 V attributed to the facilitated electron transfer kinetics-provoked synergistic interaction of $Ni(OH)_2$ and CF constituents. After the incorporation of non-metallic Se and P into the $Ni(OH)_2$ phase, the NS-CF@NCW and NSP-CF@NCW probes illustrated more amplified current responses as oxidation waves located at E_{pa} of 0.53 and 0.47 V, respectively. This remarkable electrochemical activity with a negative drift in the oxidative potential is associated with multiple factors including the modulation of the electronic framework of catalytically active architectures with distinct heterointerfaces, doping of electronically dynamic non-metallic constituents, and augmentation of the exposed active surface area evolved along with the microstructural tuning.

The electrocatalytic assessment of bare and modified probes towards urea sensing is executed in the presence of 2 mM urea under the alkaline condition (Fig. 4B). Evidently, the unmodified bare and CF@NCW probe illustrates a trivial electrocatalytic activity, whereas $Ni(OH)_2$@NCW exhibited significant performance toward urea determination. This augmented electrocatalytic behavior affirms the unambiguous role of Ni-based electrocatalytic microstructures in catalyzing the urea electro-decomposition allied with the OH^- ions, which plays a pivotal role in facilitating the reversible electrochemical transformation of Ni^{3+} from Ni^{2+}, as given in eqn (1) and (2):

$$6Ni(OH)_2 + 6OH^- \rightleftarrows 6NiOOH + 6H_2O + 6e^- \quad (1)$$

$$6NiOOH + CO(NH_2)_2 + H_2O \rightarrow 6Ni(OH)_2 + N_2 + CO_2 \quad (2)$$

Further, to examine whether the interfacial docking of $Ni(OH)_2$ over the CF composite cubes enhances the sensing activity, the analogous electrocatalytic examination was executed. Excitingly, as depicted in Fig. 4B, the $Ni(OH)_2$-CF@NCW probe exhibits notable performance elevation compared to both the CF@NCW and $Ni(OH)_2$@NCW electrodes alone. The establishment of a heterointerface between the CF composite and $Ni(OH)_2$ architectures synergistically provoked the electron distribution from former to latter, which eventually altered the local electronic framework of the Ni-phase to the new equilibrium state and profoundly triggered the surface catalytic active sites towards excellent electrocatalytic kinetics. After the incorporation of Se into the $Ni(OH)_2$ architectures, NS-CF@NCW exhibited a marked current augmentation holding a well-defined oxidative signature located at E_{pa} of 0.65 V. This electrocatalytic amplification can be attributed to the doping of Se, which endorses the effectual partial charge transfer activation on the pristine $Ni(OH)_2$ phase (as evidenced by the XPS plot, Fig. 3D), and hastens the pre-oxidation of catalytically dynamic Ni^{3+} from Ni^{2+}, thereby increasing its positive valency resulting in the increased sensing activity. Moreover, in addition to the positive influence on electron transfer kinetics, this heteroatom engineering also elevates the electrode–electrolyte interaction characteristics by increasing the roughness of NS microstructures for effective urea sensing. Astonishingly, after the integration of P constituents, the NSP-CF@NCW probe demonstrates its excellent sensing performance with a pronounced oxidation wave at E_{pa} of 0.59 V. In agreement with

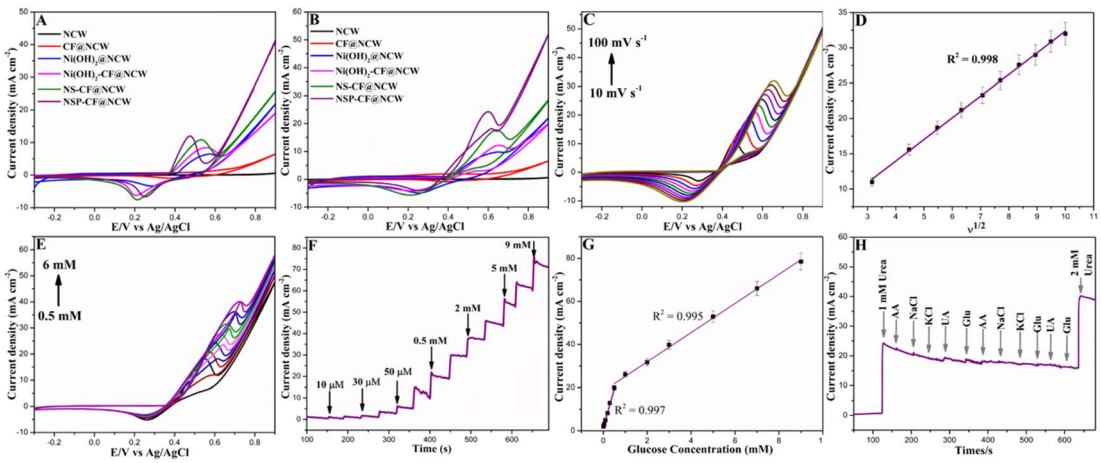

Fig. 4 CVs of the studied NCWs in (A) 0.1 M KOH, and (B) 2 mM urea and 0.1 M KOH at a scan rate of 50 mV s^{-1}. (C) CVs of NSP-CF@NCW at different scan rates in 2 mM urea and 0.1 M KOH. (D) Plot of anodic response *vs.* square root of sweep rate. CVs of NSP-CF@NCW (E) upon increment of 0.5–6.0 mM urea in 0.1 M KOH. (F) Amperometric *i*–*t* plot of NSP-CF@NCW upon successive inclusion of urea at 0.6 V *vs.* Ag/AgCl. (G) Plot of amperometric responses of NSP-CF@NCW *vs.* urea concentration. (H) Anti-interference examination of the NSP-CF@NCW sensing probe.

the XPS profile, the introduction of P as a non-metallic dopant triggers the charge transfer characteristics from Ni to P, which consequentially modulates the surface electronic configuration of catalytically active sites to possess more positive valency and unique electron transfer pathway, resulting in the enhancement of urea detection efficiency. The binder-free construction of NSP-CF over the highly conductive and porous carbon multichannels of NCW diminished the dead volume and eliminated the electron transfer resistance provoked by the utilization of insulating binders. Moreover, the dual-anion engineering of NSP walls with P and Se atoms guaranteed the rapid diffusion, accommodation, and momentous electrooxidation of urea molecules at the 3D capacious, sharp, and intertwined rough walls of NSP, which feature the best sensing activity of NSP-CF@NCW amid the other fabricated electrodes.

The exploration of the effect of varying scan rates on the electrochemical performance of NSP-CF@NCW unveiled the fundamental electrode/electrolyte interaction occurring on its surface under the alkaline medium. The CV plots (Fig. 4C) recorded at different sweep rates (ν) from 10 to 100 mV s^{-1} illustrate the linearly advancing current (I_{pa}) values. With the elevated correlation coefficient value of $R^2 = 0.998$, the profile of I_{pa} *vs.* $\nu^{1/2}$ (Fig. 4D) shows a linear scale and affirms that the electrocatalytic process engaged at NSP-CF@NCW is diffusion-guided. Fig. 4E depicts the CV responses of NSP-CF@NCW examined with the injection of distinct urea concentrations ranging from 0.5 to 6 mM at 50 mV s^{-1}. An apparent rise in the anodic responses with the gradual increment of urea concentration without the electrode fouling behavior manifests the excellent electrocatalytic activity of NSP-CF@NCW towards urea sensing. The amperometric current–time (i–t) examination of NSP-CF@NCW towards urea oxidation is further explored to assess its sensing behavior at 0.6 V *vs.* Ag/AgCl, as shown in Fig. 4F. Upon successive inclusion of urea with distinct concentrations, the amperometric response of NSP-CF@NCW toward urea detection displays the well-defined step-by-step staircase-like current augmentations. In addition, the plot of current *vs.* urea concentration (Fig. 4G) depicts the linear response in the range of 0.01–0.5 mM and 0.5–9.0 mM with the corresponding highest sensitivities of 33.1 and 7.0 mA mM^{-1} cm^{-2} and a lower limit of detection (LOD) of 0.0085 mM estimated with a signal-to-noise ratio value of 3 (S/N = 3). Besides, the as-constructed NSP-CF@NCW sensing probe surpasses the sensing characteristics of reported EFUSs, as given in Table S1.† In alliance with the interfacial and multi-elemental electronic effects, the highly capacious and rough cactus-like NSP microflakes with a well-interconnected framework built over the CF cubes docked upon the NCW platform flourished the EFUS kinetics momentously. The anti-interference property of the constructed urea sensing probe is a crucial analytical factor for its real-world implementation. Thus, the assessment of the anti-interference behavior of NSP-CF@NCW (Fig. 4H) was performed *via* amperometric scrutiny with the inclusion of potential ionic and biological interferents such as KCl, NaCl, glucose, uric acid, and ascorbic acid in the concentration of 0.1 mM. An obvious current increase after injection of urea is observed, followed by a steady-state amperometric signal with a trivial response towards the addition of potential interferents. However, a marked signal increment was detected after the inclusion of the target analyte, validating the excellent selectivity of NSP-CF@NCW towards urea.

Reproducibility, stability, and real-sample analysis

The reproducibility features of the fabricated probe were evaluated with the five different NSP-CF@NCW electrodes fabricated under identical conditions. As shown in Fig. S6A and B,† all the built NSP-CF@NCWs showed significant electrode-to-electrode reproducibility properties with a relative standard deviation (RSD) range of 1.5%. The prolonged storage stability of the prepared sensors was examined by evaluating the electrochemical behavior of NSP-CF@NCW electrodes after being kept in the ambient conditions, and the results (Fig. S6C†) indicate that all the fabricated electrodes exhibited good shelf life with a minimum variation of 2.9% assessed by day-by-day analysis, affirming their admirable stability. The analytical feasibility of the developed sensor toward the real sample was studied with the urea determination in urine samples obtained from a healthy donor and labeled as 1 and 2 after the filtering procedure to remove the protein clumps. The samples obtained are diluted with 0.1 M KOH to examine the current behavior of the prepared sensor toward the given concentration of urea. With significant recovery values of 96.0–99.0% (Table S2†), the as-prepared NSP-CF@NCW sensing probe endorsed its practical viability for real sample examination.

Electrochemical performance of the fabricated electrodes towards UOR

The electrocatalytic UOR performances of NSP-CF@NCW and its counterparts (NCW, CF@NCW, $Ni(OH)_2$@NCW, $Ni(OH)_2$-CF@NCW, and NS-CF@NCW) were exploited in a standard three-electrode configuration with 1.0 M KOH containing 0.33 M urea (to mimic the urea concentration in urine). Fig. 5A shows the LSV plots of NSP-CF@NCW in various electrolytes. In the presence of 1.0 M KOH, NSP-CF@NCW delivers a higher current figure (100 mA cm^{-2}) at an elevated potential (E_{100}) of 1.71 V (*vs.* RHE), whereas, after the inclusion of 0.33 M urea, with a small onset potential of 1.29 V, NSP-CF@NCW demonstrates a brilliant drift in E_{100} towards the lower potential value positioned at 1.40 V (*vs.* RHE) to drive the abovementioned current density, which is 310 mV efficient than the conventional OER reflecting the high performance and superiority of this anode towards UOR. Moreover, the comparative UOR examination of NSP-CF@NCW with other catalyst-modified electrodes (Fig. 5B) reveals that the best-performing electrode holds E_{100} values of 110, 230, 440, and 750 mV lower than that of NS-CF@NCW, $Ni(OH)_2$-CF@NCW, $Ni(OH)_2$@NCW, and CF-@NCW, respectively. It manifests that the greatly exposed 3D surface of well-interconnected capacious and rough flaky architectures that are electronically re-engineered by the doping non-metallic Se and P into Ni skeletons momentously elevated the UOR kinetics of NSP-CF@NCW. The additional kinetic investigations of prepared electrodes towards the UOR were evaluated using their equivalent Tafel plots. As shown in

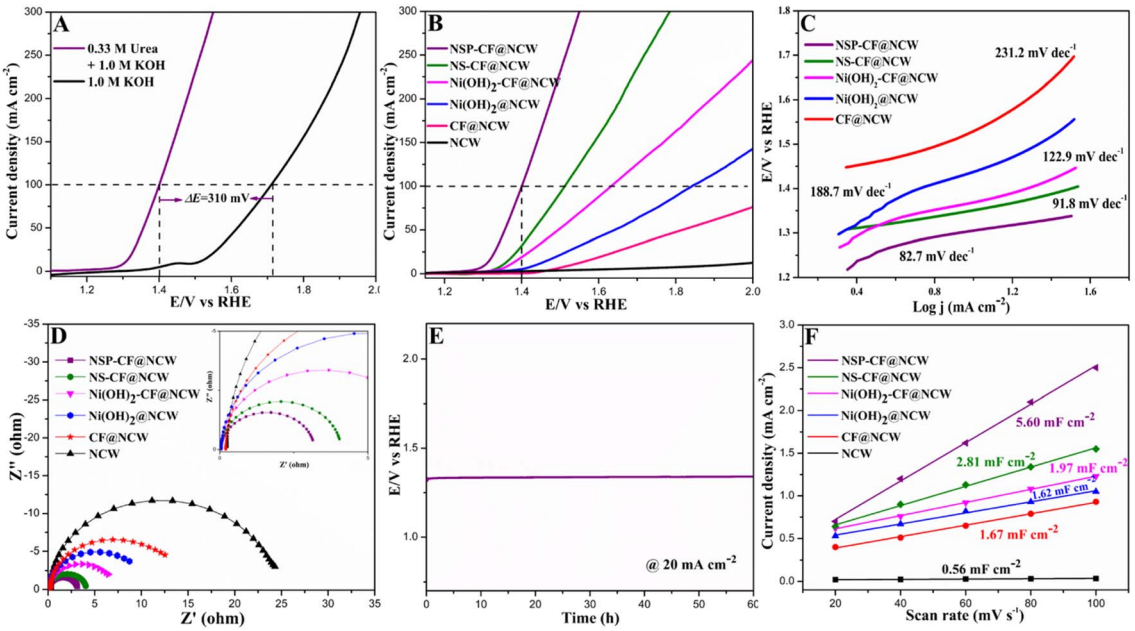

Fig. 5 (A) LSV curves for the OER and UOR of NSP-CF@NCW in 1.0 M KOH and 0.33 M urea + 1.0 M KOH at a scan rate of 5 mV s^{-1}. (B) UOR LSVs of all the studied NCWs, (C) the related Tafel slopes, (D) and Nyquist profiles of all the fabricated electrodes in 0.33 M urea + 1.0 M KOH. (E) Chronopotentiometric profile of NSP-CF@NCW at 20 mA cm^{-2} in 0.33 M urea + 1.0 M KOH. (F) C_{dl} values of all the studied anodes.

Fig. 5C, NSP-CF@NCW illustrates a smaller Tafel slope value (82.7 mV dec^{-1}) than that of NS-CF@NCW (91.8 mV dec^{-1}), $Ni(OH)_2$-CF@NCW (122.9 mV dec^{-1}), $Ni(OH)_2$@NCW (188.7 mV dec^{-1}) and CF@NCW (231.2 mV dec^{-1}), which obviously verifies that NSP-CF@NCW possess the fastest UOR kinetics.

In addition, the dynamic charge transfer properties occurring at the interface of the electrode and electrolyte were studied with EIS plots for the prepared electrodes under the electrolytic combination of 0.33 M urea and 1.0 M KOH, as shown in Fig. 5D (equivalent circuit diagram provided in Fig. S7†). Among the impedance profiles, the Nyquist plot for the unmodified NCW reveals the highest charge transfer resistance (R_{ct}) of 24.4 Ω, whereas the catalyst-modified electrodes illustrate a lowering trend of R_{ct} characteristics, implying the crucial role of electroactive architectures. The lowest R_{ct} value acquired for NSP-CF@NCW (3.15 Ω) compared with its counterparts agrees with its exceptional electrocatalytic activity and adds more validation to its brilliant charge transfer characteristics towards UOR. Besides, in contrast to NCW and CF@NCW, the pronounced UOR characteristics of $Ni(OH)_2$@NCW, $Ni(OH)_2$-CF@NCW, NS-CF@NCW, and NSP-CF@NCW infer the inevitable influence of Ni active species as dynamic electrocatalytic sites for the electrodecomposition of urea. With high catalytic activity, the concrete electrochemical stability of NSP-CF@NCW toward the UOR in a harsh alkaline environment is another vital parameter for its widespread practical implementation. In the presence of 0.33 M urea and 1.0 M KOH, the chronopotentiometric response depicted in Fig. 5E shows that the NSP-CF@NCW anode displayed excellent endurance over time and validated its robustness towards UOR. Besides, as shown in Fig. S8A,† NSP-CF@NCW illustrated excellent cycling stability even after 2000 CV cycles. Concurrently, XRD and SEM measurements were carried out to examine the chemical and structural stability of the best-performing electrode (Fig. S8B–D†), which portrays nominal structural and chemical deformations. The above-mentioned studies affirmed the exceptional long-term and cycling stability of NSP-CF@NCW. This sustained stability of the NSP-CF@NCW anode in the challenging alkaline medium was rendered by the binder-free construction of catalytically dynamic microstructures over the NCW scaffold. Besides, the brilliant UOR activity of NSP-CF@NCW was supported by the electrochemically active surface area proportional to the double-layer capacitance (C_{dl}) of the constructed electrode obtained from its CV curves executed at various sweep rates (Fig. S9†) in the potential window of the non-faradaic region. Fig. 5F discloses that the C_{dl} value of NSP-CF@NCW (5.60 mF cm^{-2}) is much larger than those of NS-CF@NCW (2.81 mF cm^{-2}), $Ni(OH)_2$-CF@NCW (1.97 mF cm^{-2}), $Ni(OH)_2$@NCW (1.62 mF cm^{-2}), CF@NCW (1.67 mF cm^{-2}), and NCW (0.56 mF cm^{-2}), illuminating that NSP-CF@NCW was equipped with much higher active site density for efficient UOR. Moreover, the intrinsic activity of the fabricated electrodes was further assessed by the normalized LSVs (Fig. S10A†) acquired by the electrochemical active surface area (ECSA) and the turnover frequency (TOF) plots (Fig. S10B†), which also manifested that the NSP-CF@NCW electrode retained its highest UOR activity among its variants.[71,72]

Electrochemical behavior of constructed electrodes toward HER

The electrocatalytic HER performance of the NSP-CF@NCW electrode was analyzed by acquiring its LSV profile in a three-electrode system comprising argon-saturated 1.0 M KOH as an electrolyte medium. The HER behavior of the other

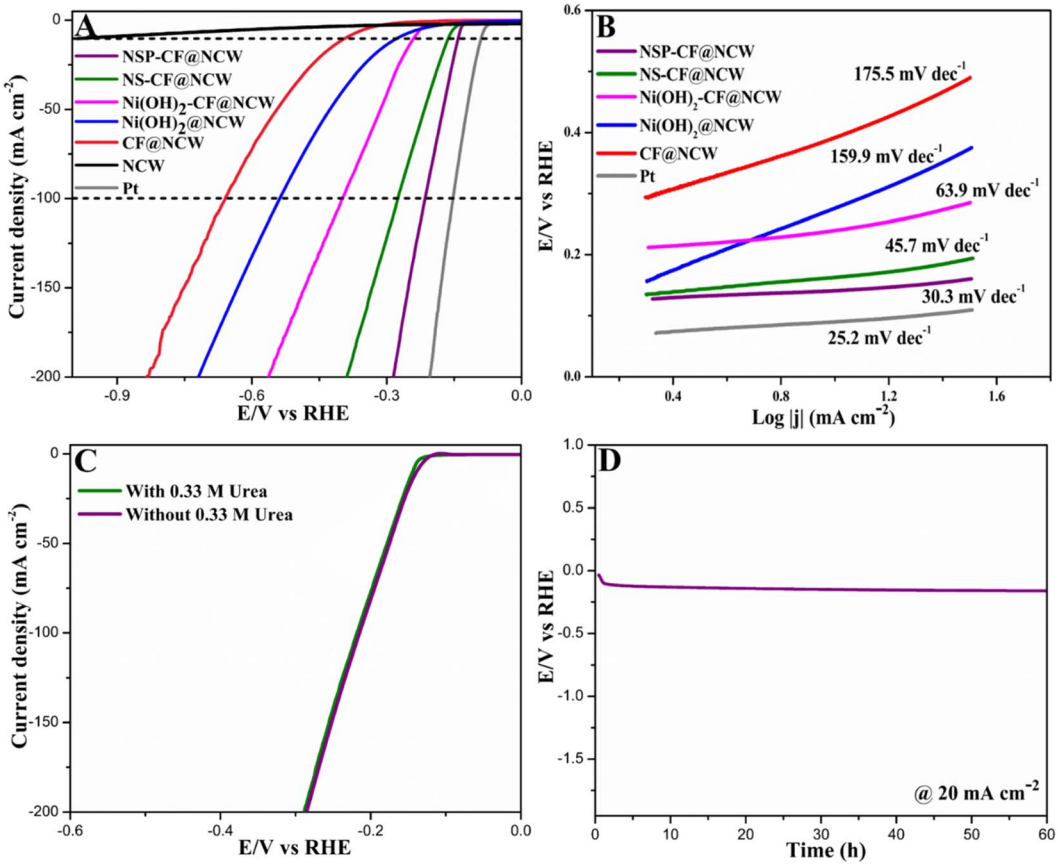

Fig. 6 (A) LSV curves for the HER of all the studied NCWs at a scan rate of 5 mV s^{-1} and (B) the related Tafel slopes. (C) LSVs of the NSP-CF@NCW cathode in 1.0 M KOH and 0.33 M urea + 1.0 M KOH. (D) Chronopotentiometric plot of the NSP-CF@NCW cathode at 20 mA cm^{-2} for the HER.

fabricated cathodes involving a commercial Pt electrode was also scrutinized for comparison. As portrayed in Fig. 6A, among the HER polarization profiles of all the catalyst-decorated electrodes, the NSP-CF@NCW cathode demonstrated remarkable HER activity by delivering a geometric current density of 10 mA cm^{-2} at a low overpotential of 0.14 V (*vs.* RHE). This value is much lower than that of NS-CF@NCW (0.16 V), $Ni(OH)_2$-CF@NCW (0.24 V), $Ni(OH)_2$@NCW (0.27 V), and CF@NCW (0.40 mV) validating the superior HER characteristics of the NSP-CF@NCW electrode. Moreover, the acquired TOF profile (Fig. S10C†) supports the elevated HER activity of the best-performing electrode. Even at the high current density figures, NSP-CF@NCW delivered comparable HER activity to the noble metal electrode, particularly at a current density of 100 mA cm^{-2}. This marked excellence of the NSP-CF@NCW cathode towards the HER activity may be attributed not only to the 3D highly exposed capacious catalytic architectures but also to the electronic modulations established by the interfacial engineering between the multi-composites and the dual docking of non-metals. The faster kinetics and the augmented catalytic HER activity of the NSP-CF@NCW electrode were further confirmed by the smaller Tafel slope value (30.3 mV dec^{-1}) than that of its other built electrodes (Fig. 6B). Moreover, the catalytic HER performance of the NSP-CF@NCW electrode was examined in an electrolytic mixture of 1.0 M KOH and 0.33 M urea to evaluate its urea tolerance behavior under the applied potential. According to Fig. 6C, the as-fabricated NSP-CF@NCW cathode delivered identical HER activity in both the presence and the absence of urea, illustrating its robust stability toward HER. The long-term durability (Fig. 6D) of the NSP-CF@NCW cathode is another pivotal index that evaluates its industrial and commercial possibilities. As shown in the chronopotentiometry plot, there is no notable sign of decay in the performance of NSP-CF@NCW under the alkaline environment at the applied current, indicating its solid durability toward HER.

Electrocatalytic activity of the fabricated electrode toward overall urea electrolysis

Inspired by the excellent UOR and HER performances together with concrete durability, an energy-efficient two-electrode urea electrolyzer was constructed using NSP-CF@NCW electrodes as bifunctional cathodes and anodes and deployed as the HER‖OER system in the presence of 0.33 M urea and 1.0 M KOH (Fig. 7A). For comparison, a conventional water electrolysis system, labeled as HER‖OER, was also exploited by employing the aforementioned symmetric two-electrode system. As depicted in Fig. 7B, the NSP-CF@NCW‖NSP-CF@NCW electrolyzer only demanded a cell voltage of 1.60 V to deliver a current density of 100 mA cm^{-2} in the HER‖UOR configuration, which is 250 mV more efficient than the conventional HER‖OER

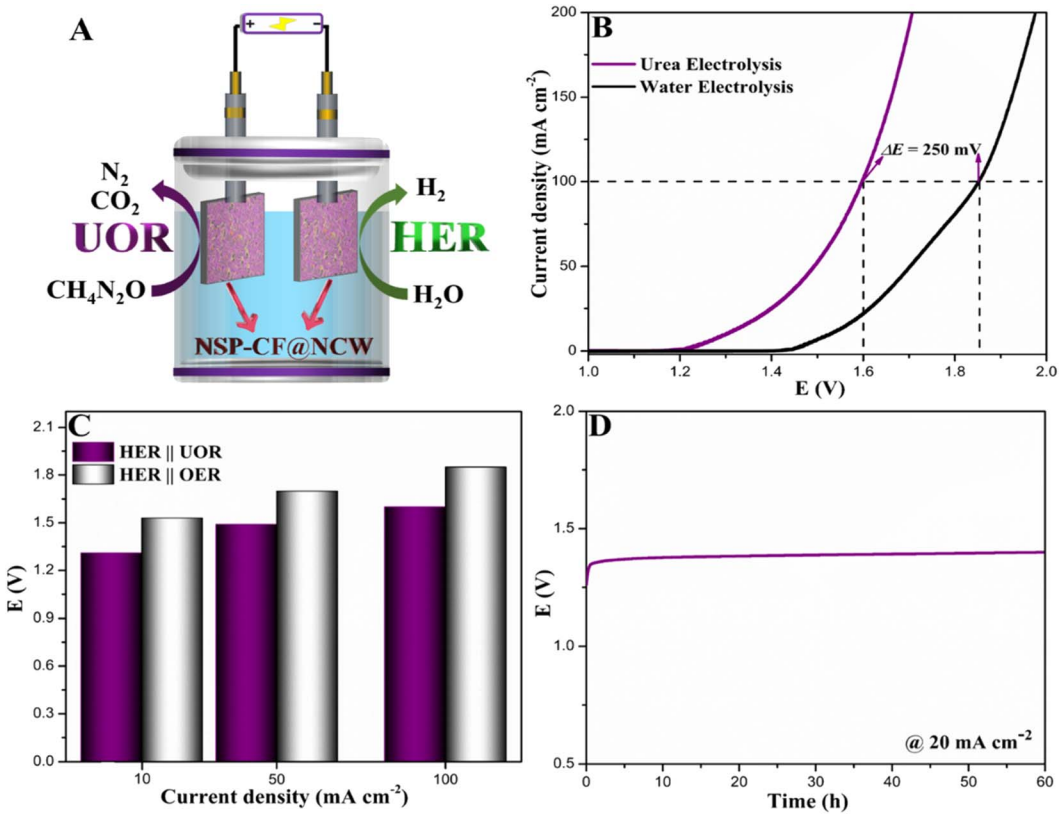

Fig. 7 (A) Schematic representation of the HER||UOR system involving NSP-CF@NCW as a bifunctional electrode. (B) LSVs of bifunctional NSP-CF@NCW electrodes in HER||UOR and HER||OER configurations. (C) Comparison plot of cell voltages of HER||UOR and HER||OER configurations at different current densities. (D) Chronopotentiometric examination at 20 mA cm^{-2} for the HER||UOR configuration containing bifunctional NSP-CF@NCW electrodes.

system, demonstrating the potential capability of the as-constructed bifunctional electrode to execute the energy conserving urea-electrolysis process. The 3D highly capacious and rough multi-element engineered NSP micro-flakes with a well-interconnected framework decorated over the CF cube composites robustly docked over the NCW platform promisingly elevated the overall urea electrolysis significantly. Besides, the interface bridging between the CF composite cubes with NSP architectures enabled the momentous electron transfer between the former and the latter, which eventually modulated the local electronic framework of NSP skeletons to the new equilibrium state and accelerated the catalytic activity of surface active sites towards excellent urea electrolysis. Similarly, the best-performing NSP-CF@NCW||NSP-CF@NCW system only requires 1.31 V and 1.49 V to harvest current densities of 10 and 50 mA cm^{-2}, respectively. Fig. 7C displays the comparative plot of current densities against the cell voltages required by the NSP-CF@NCW||NSP-CF@NCW configuration in HER||UOR and HER||OER systems. Table S3† shows the outstanding performance of NSP-CF@NCW as a bifunctional urea electrolyzer electrode in comparison with those reported in the literature. To further validate the efficiency of the aforementioned bifunctional electrode system to execute long-term urea electrolysis, the endurance of the symmetric NSP-CF@NCW||NSP-CF@NCW configuration was assessed by chronopotentiometry, as displayed in Fig. 7D. As shown in the stability plot, the best-performing symmetric electrode configuration demonstrated long-term operational durability at a current density of 20 mA cm^{-2}, indicating its robust endurance towards overall urea electrolysis.

Besides, we further explored the practical efficiency of the as-constructed NSP-CF@NCW||NSP-CF@NCW configuration towards urea electrolysis in real-world samples including human urine, domestic wastewater, and agricultural wastewater (Fig. 8A–C). In the presence of 1.0 M KOH, the NSP-CF@NCW||NSP-CF@NCW system demonstrates excellent urea electrolysis activity in the human urine (Fig. 8A) by requiring only 1.66 V to deliver a current density of 100 mA cm^{-2}, which is comparable to the LSV profile obtained using the electrolyte of 1.0 M KOH and 0.33 M urea. However, in domestic wastewater (Fig. 8B), the constructed urea electrolysis system delivered nominal catalytic activity (1.89 V to deliver 100 mA cm^{-2}) owing to the presence of other chemical interferents and insignificant levels of urea. In contrast, as displayed in Fig. 8C, the NSP-CF@NCW||NSP-CF@NCW electrode delivered excellent performance towards urea electrolysis in the agricultural wastewater solution by requiring 1.77 V to deliver the abovementioned current figure, which is 120 mV lower than that required for domestic wastewater electrolysis. This performance augmentation can be ascribed to the significant levels of fertilizer urea present in agricultural wastewater. Moreover, the chronopotentiometry profiles obtained for the NSP-CF@NCW||NSP-

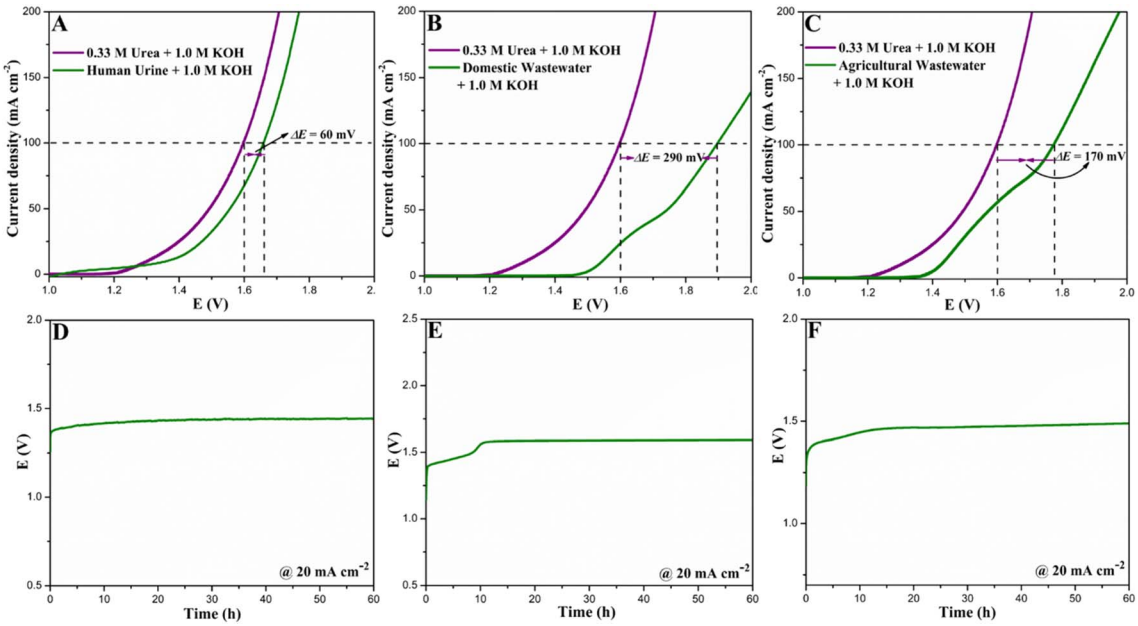

Fig. 8 LSV curves and chronopotentiometric plots of bifunctional NSP-CF@NCW electrodes in (A and D) human urine, (B and E) domestic wastewater, and (C and F) agricultural wastewater.

CF@NCW configuration in human urine, domestic wastewater, and agricultural wastewater are depicted in Fig. 8D–F. Even though the stability plots display an initial decay associated with the fouling of catalytic active sites by other organic constituents in the abovementioned samples, the NSP-CF@NCW‖NSP-CF@NCW electrodes exhibit significant steady-state behavior over the progress of time. The above-mentioned experiments promisingly illustrate the possibility of practical deployment of bifunctional NSP-CF@NCW‖NSP-CF@NCW electrodes to simultaneously perform energy-efficient power-to-fuel production and wastewater treatment.

The outstanding trifunctional electrocatalytic performance of the NSP-CF@NCW electrode towards both sensing and energy-conserving urea electrolysis is more substantiated for the following reasons: (1) the strategic integration of catalytically vibrant $Ni(OH)_2$ microarchitectures with CF composite cubes profoundly establishes a unique heterojunction interface that modulates the electronic framework of Ni by sharing the electron density, which constructively resulted in the electrocatalytic amplification. (2) Further incorporation of non-metallic constituents including Se followed by P triggered the electron-level re-engineering aided by the partial charge transfer activation on the pristine $Ni(OH)_2$ phase to possess more positive valency, which concurrently accelerated the pre-oxidation Ni^{3+} from Ni^{2+} of $Ni(OH)_2$ in an Ni^{2+} in the alkaline environment and brilliantly augmented the UOR kinetics of NSP-CF@NCW. (3) In addition to the inherent microstructural merits of robustly rooted $Ni(OH)_2$ phase over the CF cubes involving a well-interconnected and highly voluminous flaky network, the high-temperature decoration of multi-elemental heteroatoms further amplified NSP-CF@NCW's porous characteristics by constructing a cactus-like morphology and upsurging the exposed surface roughness, which remarkably accelerated the diffusion, adsorption and utilization of target molecules/ions at the electrified interface and elevated the trifunctional electroactivity of the best-performing electrode. (4) The implementation of a binder-free approach to construct the catalytically dynamic NSP-CF over the sustainable NCW support not only eliminated the binder-mediated electron transfer resistance that obstructed the effective multifaceted electrocatalysis but also afforded the concrete stability during the electrochemical assessments.

Conclusion

In summary, a trifunctional, binder-free, self-standing, and sustainable NSP-CF@NCW electrode with 3D Se and P-fused NSP microflakes rationally integrated with CF composite cubes grown on the naturally voluminous carbon multi-channels of NCW using the cost-effective diverse fabrication protocols has illustrated its excellent performance toward EFUS and urea-assisted water electrolysis compared to its other variants. The NSP-CF@NCW sensor used for urea detection exhibits remarkable sensitivities of 33.1 and 7.0 mA mM^{-1} cm^{-2}, covering extensive linear ranges of 0.01–0.5 mM and 0.5–9.0 mM, respectively, with an impressive detection limit of 0.0085 mM (S/N = 3). Further, as a urea electrolyzer, the most proficient NSP-CF@NCW‖NSP-CF@NCW electrode configuration achieves high current densities of 50 and 100 mA cm^{-2} at overpotentials of merely 1.49 and 1.60 V, respectively. This eminent multifaceted electrocatalytic activity of NSP-CF@NCW was triggered by the distinct electron framework and microstructural engineering of electrocatalytic sites executed with the establishment of a unique heterojunction interface and multi-elemental decorations was explored with diverse electrochemical examinations and its corresponding inferences are

presented. This research effort not only opens a new avenue for the development and advancement of trifunctional self-sustaining electrodes for the highly demanded analytical and green-energy conversion technologies by precisely tailoring the multi-component electrocatalytic active structures but also provides insights into the construction of multifunctional electrodes that hold the potential to reduce the cost of fabrication, conserves energy and promotes the commercialization of impressive electrochemical technologies.

Author contributions

Ameer Farithkhan: conceptualization, data curation, formal analysis, investigation, methodology, writing – original draft. N. S. K. Gowthaman: investigation, validation, writing – review & editing. Raju Suresh Kumar: formal analysis. Krishnapandi Alagumalai: formal analysis. Wei Sea Chang: writing – review & editing. S. Meenakshi: project administration, supervision, validation, writing – review & editing.

Conflicts of interest

There are no conflicts to declare.

Acknowledgements

We are grateful to Prof. S. Abraham John, Department of Chemistry, The Gandhigram Rural Institute – Deemed to be University for providing an electrochemical workstation facility. N. S. K. Gowthaman is thankful to the Internal Research Grant (STG-00057) from Monash University Malaysia, Malaysia. This project was supported by the Researchers Supporting Project number (RSP2024R142), King Saud University, Riyadh, Saudi Arabia.

References

1 S. Sanati, A. Morsali and H. García, *Energy Environ. Sci.*, 2022, **15**, 3119–3151.
2 P. Li, G. H. Lee, S. Y. Kim, S. Y. Kwon, H. R. Kim and S. Park, *ACS Nano*, 2021, **15**, 1960–2004.
3 H. Sun, X. Xu, H. Kim, W. C. Jung, W. Zhou and Z. Shao, *Energy Environ. Mater.*, 2023, **6**, e12441.
4 A. L. Gropman, M. Summar and J. V. Leonard, *J. Inherited Metab. Dis.*, 2007, **30**, 865–879.
5 M. Tyagi, M. Tomar and V. Gupta, *Biosens. Bioelectron.*, 2013, **41**, 110–115.
6 A. Hilding-Ohlsson, J. A. Fauerbach, N. J. Sacco, M. C. Bonetto and E. Cortón, *Sensors*, 2012, **12**, 12220–12234.
7 K. N. Fatema, C. H. Jung, Y. Liu, S. Sagadevan, K. Y. Cho and W. C. Oh, *ACS Biomater. Sci. Eng.*, 2020, **6**, 6981–6994.
8 J. C. Chen, J. C. Chou, T. P. Sun and S. K. Hsiung, *Sens. Actuators, B*, 2003, **91**, 180–186.
9 P. Arul, N. S. K. Gowthaman, S. A. John and S. T. Huang, *Mater. Chem. Front.*, 2021, **5**, 1942–1952.
10 Y. Wang, Y. Zhang, Y. Wang, R. Zhu, Y. Chen, X. Liu, J. Xu, M. Li and D. Wang, *Electroanalysis*, 2021, **33**, 2406–2416.
11 S. Amin, A. Tahira, A. Solangi, V. Beni, J. R. Morante, X. Liu, M. Falhman, R. Mazzaro, Z. H. Ibupoto and A. Vomiero, *RSC Adv.*, 2019, **9**, 14443–14451.
12 S. Mondal and M. V. Sangaranarayanan, *Sens. Actuators, B*, 2013, **177**, 478–486.
13 M. Arain, A. Nafady, Sirajuddin, Z. H. Ibupoto, S. T. Hussain Sherazi, T. Shaikh, H. Khan, A. Alsalme, A. Niaz and M. Willander, *RSC Adv.*, 2016, **6**, 39001–39006.
14 M. Vidotti, M. R. Silva, R. P. Salvador, S. I. C. de Torresi and L. H. Dall'Antonia, *Electrochim. Acta*, 2008, **53**, 4030–4034.
15 X. Tao, H. Xu, S. Luo, Y. Wu, C. Tian, X. Lu and Y. Qing, *Appl. Catal., B*, 2020, **279**, 119367–119375.
16 B. Zhou, Y. Liu, X. Wu, H. Liu, T. Liu, Y. Wang, S. Mehdi, J. Jiang and B. Li, *Nano Res.*, 2022, **15**, 1415–1423.
17 H. Zhang, S. Min, F. Wang and Z. Zhang, *Dalton Trans.*, 2020, **49**, 15607–15611.
18 P. Zhang, Y. Liu, S. Wang, L. Zhou, T. Liu, K. Sun, H. Cao, J. Jiang, X. Wu and B. Li, *Small*, 2022, **18**, 2202725.
19 Y. Liu, K. Zhang, K. Wang, M. Wang, Y. Liu, J. Jiang, T. Liu, E. Liang and B. Li, *Appl. Catal., B*, 2022, **318**, 121890.
20 R. Shen, Y. Liu, H. Zhang, S. Liu, H. Wei, H. Yuan, H. Wen, X. Wu, S. Mehdi, T. Liu, J. Jiang, E. Liang and B. Li, *Appl. Catal., B*, 2023, **328**, 122484.
21 H. Zhang, H.-C. Chen, S. Feizpoor, L. Li, X. Zhang, X. Xu, Z. Zhuang, Z. Li, W. Hu, R. Snyders, D. Wang and C. Wang, *Adv. Mater.*, 2024, 2400523.
22 Z. Y. Yu, Y. Duan, X. Y. Feng, X. Yu, M. R. Gao and S. H. Yu, *Adv. Mater.*, 2021, **33**, 2007100.
23 J. Yu, X. Du, H. Liu, C. Qiu, R. Yu, S. Li, J. Ren and S. Yang, *Energy Fuels*, 2021, **35**, 19000–19011.
24 P. J. McHugh, A. D. Stergiou and M. D. Symes, *Adv. Energy Mater.*, 2020, **10**, 2002453.
25 Z. Wu, Y. Zhao, H. Wu, Y. Gao, Z. Chen, W. Jin, J. Wang, T. Ma and L. Wang, *Adv. Funct. Mater.*, 2021, **31**, 2010437.
26 R. K. Singh, K. Rajavelu, M. Montag and A. Schechter, *Energy Technol.*, 2021, **9**, 2100017.
27 B. Zhu, Z. Liang and R. Zou, *Small*, 2020, **16**, 1906133.
28 C. J. Huang, H. M. Xu, T. Y. Shuai, Q. N. Zhan, Z. J. Zhang and G. R. Li, *Small*, 2023, **19**, 2301130.
29 B. K. Boggs, R. L. King and G. G. Botte, *Chem. Commun.*, 2009, 4859–4861.
30 V. Vedharathinam and G. G. Botte, *Electrochim. Acta*, 2013, **108**, 660–665.
31 X. Wang, P. Zhao, L. Ling, Y. Luo, Z. Li, Z. Jiao and L. Cheng, *J. Alloys Compd.*, 2022, **927**, 166845.
32 C. Liu, T. Gong, J. Zhang, X. Zheng, J. Mao, H. Liu, Y. Li and Q. Hao, *Appl. Catal., B*, 2020, **262**, 118245.
33 Y. Pan, M. Wang, M. Li, G. Sun, Y. Chen, Y. Liu, W. Zhu and B. Wang, *J. Energy Chem.*, 2022, **68**, 699–708.
34 C. T. Zeng, L. Dai, Y. H. Jin, J. B. Liu, Q. Q. Zhang and H. Wang, *Sustainable Energy Fuels*, 2021, **5**, 1347–1365.
35 M. Maleki, A. Sabour Rouhaghdam, G. Barati Darband, D. Han, M. Chehelamirani and S. Shanmugam, *J. Electroanal. Chem.*, 2022, **916**, 116379.
36 Z. Pu, T. Liu, I. S. Amiinu, R. Cheng, P. Wang, C. Zhang, P. Ji, W. Hu, J. Liu and S. Mu, *Adv. Funct. Mater.*, 2020, **30**, 2004009.

37 S. Xu, X. Yu, L. Luo, W. Li, Y. Du, Q. Kong and Q. Wu, *Nano Res.*, 2022, **15**, 4942–4949.
38 B. Yang, X. Chang, X. Ding, X. Ma and M. Zhang, *J. Colloid Interface Sci.*, 2022, **623**, 196–204.
39 H. Xu, H. Shang, C. Wang and Y. Du, *Coord. Chem. Rev.*, 2020, **418**, 213374.
40 G. Zhao, Y. Jiang, S. X. Dou, W. Sun and H. Pan, *Sci. Bull.*, 2021, **66**, 85–96.
41 P. Wang and B. Wang, *ACS Appl. Mater. Interfaces*, 2021, **13**, 59593–59617.
42 H. Yi, S. Liu, C. Lai, G. Zeng, M. Li, X. Liu, B. Li, X. Huo, L. Qin, L. Li, M. Zhang, Y. Fu, Z. An and L. Chen, *Adv. Energy Mater.*, 2021, **11**, 2002863.
43 Y. Wang, M. Zhang, Y. Liu, Z. Zheng, B. Liu, M. Chen, G. Guan and K. Yan, *Adv. Sci.*, 2023, **10**, 2207519.
44 G. Sharma, D. Kumar, A. Kumar, A. H. Al-Muhtaseb, D. Pathania, M. Naushad and G. T. Mola, *Mater. Sci. Eng., C*, 2017, **71**, 1216–1230.
45 S. Sanati, R. Abazari, J. Albero, A. Morsali, H. García, Z. Liang and R. Zou, *Angew. Chem., Int. Ed.*, 2021, **60**, 11048–11067.
46 A. A. Kashale, C. H. Yi, K. Y. Cheng, J. S. Guo, Y. H. Pan and I. W. P. Chen, *ACS Appl. Energy Mater.*, 2020, **3**, 10831–10840.
47 J. Qian, Y. Zhang, Z. Chen, Y. Du and B. J. Ni, *Chemosphere*, 2023, **345**, 140472.
48 F. Guo, K. Cheng, K. Ye, G. Wang and D. Cao, *Electrochim. Acta*, 2016, **199**, 290–296.
49 S. Hu, C. Xiang, Y. Zou, F. Xu and L. Sun, *Nanomaterials*, 2023, **13**, 1871.
50 J. Yang, H. Xuan, J. Yang, X. Liang, Y. Li, J. Yang and P. Han, *J. Alloys Compd.*, 2023, **934**, 167908.
51 J. Qu, Z. Wang, W. Gan, R. Xiao, X. Yao, Z. Khanam, L. Ouyang, H. Wang, H. Yang, S. Zhang and M. S. Balogun, *Small*, 2024, **20**, 202304541.
52 R. Xiao, F. Wang, L. Luo, X. Yao, Y. Huang, Z. Wang and M. S. Balogun, *Small Methods*, 2023, **7**, 2201659.
53 J. Li, Z. Zhu, Y. Huang, F. Wang and M. S. Balogun, *Mater. Today Energy*, 2022, **26**, 101001.
54 T. Xiong, J. Li, J. C. Roy, M. Koroma, Z. Zhu, H. Yang, L. Zhang, T. Ouyang, M. S. Balogun and M. Al-Mamun, *J. Energy Chem.*, 2023, **81**, 71–81.
55 Q. Meng, H. Ge, W. Yao, W. Zhu and T. Duan, *New J. Chem.*, 2019, **43**, 3649–3652.
56 J. Yang, Y. Chen, P. Xu, Y. Li, X. Jia and H. Song, *Mater. Lett.*, 2019, **254**, 210–213.
57 M. Bhavanari, K. R. Lee, C. J. Tseng, I. H. Tang and H. H. Chen, *Int. J. Hydrogen Energy*, 2021, **46**, 35886–35895.
58 X. Xing, Y. Song, W. Jiang and X. Zhang, *Sustainable Energy Fuels*, 2020, **4**, 3985–3991.
59 Y. Yang, L. Li, B. Luosang, M. Shao and X. Fu, *ChemistrySelect*, 2021, **6**, 5218–5224.
60 Y. Huang, L. W. Jiang, X. L. Liu, T. Tan, H. Liu and J. J. Wang, *Appl. Catal., B*, 2021, **299**, 120678.
61 Y. Huang, L. W. Jiang, B. Y. Shi, K. M. Ryan and J. J. Wang, *Adv. Sci.*, 2021, **8**, 2101775.
62 A. I. Inamdar, H. S. Chavan, B. Hou, C. H. Lee, S. U. Lee, S. N. Cha, H. Kim and H. Im, *Small*, 2020, **16**, 1905884.
63 Y. M. Wang, D. D. Zhao, Y. Q. Zhao, C. L. Xu and H. L. Li, *RSC Adv.*, 2012, **2**, 1074–1082.
64 X. Xu, R. Wang, S. Chen, A. Trukhanov, Y. Wu, L. Shao, L. Huang and Z. Sun, *Inorg. Chem. Front.*, 2022, **9**, 5507–5516.
65 Z. Li, O. Zabihi, J. Wang, Q. Li, J. Wang, W. Lei and M. Naebe, *RSC Adv.*, 2017, **7**, 2621–2628.
66 J. Zhao, Z. Li, X. Yuan, Z. Yang, M. Zhang, A. Meng and Q. Li, *Adv. Energy Mater.*, 2018, **8**, 1702787.
67 C. Hao, F. Wen, J. Xiang, L. Wang, H. Hou, Z. Su, W. Hu and Z. Liu, *Adv. Funct. Mater.*, 2014, **24**, 6740.
68 Z. Chen, T. Zhou, Z. Wang, J. Tao, R. Gu and Y. Liu, *Energy Fuels*, 2023, **37**, 13296–13304.
69 W. Zhao, S. Wang, C. Feng, H. Wu, L. Zhang and J. Zhang, *ACS Appl. Mater. Interfaces*, 2018, **10**, 40491–40499.
70 B. C. Chen, X. Lu, H. Y. Zhong, P. W. Huang, Y. N. Wu, S. Y. Xu, K. Z. Du and X. H. Wu, *J. Mater. Chem. A*, 2022, **10**, 25671–25682.
71 T. Xiong, Z. Zhu, Y. He, M. S. Balogun and Y. Huang, *Small Methods*, 2023, **7**, 2201472.
72 Z. Zhu, L. Luo, Y. He, M. Mushtaq, J. Li, H. Yang, Z. Khanam, J. Qu, Z. Wang and M. S. Balogun, *Adv. Funct. Mater.*, 2024, **34**, 2306061.